Stochastic rock physics modeling for seismic anisotropy

Yunyue (Elita) Li, Biondo Biondi, Dave Nichols, Gary Mavko, and Robert Clapp

ABSTRACT

Anisotropic model building using surface seismic data is a well-known underdetermined and nonlinear problem. To stabilize the inversion, a regularization term is often added into the data fitting objective function assuming a priori anisotropic model. In this paper, we build the anisotropic prior model using stochastic rock physics modeling for shale anisotropy. We consider shale anisotropy from four aspects: mineral elastic anisotropy for the constitutes of the rock, the mineral transition due to compaction and temperature, particle alignment during compaction and shale/sand lamination. The input parameters for the rock physics modeling are provided by two different sources: quantitative inversion results from seismic impedance in three dimensional space and well-log measurements at isolated well locations. For each instance of modeling, we perturb the key parameters for the rock physics modeling to produce a set of random models. The modeling results are compared at three different depth levels in a statistical manner. The similarity between both modeling results justifies the use of the seismic inversion results in the deeper region that the well logs do not cover. To better utilize the seismic and the rock physics information, we also propose a new parameterization scheme for wave-equation migration velocity analysis.

INTRODUCTION

Anisotropic model building tries to resolve more than one parameter at each grid point of the subsurface. This number could be three for a vertical transverse isotropic (VTI) media, and increases to five for a tilted transverse isotropic (TTI) media. Any inversion scheme based on surface seismic data only becomes ill-posed and highly underdeterimined due to the rapidly increasing model space with the increasing complexity of the subsurface.

One big disadvantage of the surface seismic inversion is its lack of depth information. To add the depth dimension into the inversion, several localized tomography studies around the wells have been performed (Bakulin et al., 2010d,c). In these studies, joint inversion of surface seismic data and borehole data (check-shots, walkaway VSPs) showed great potentials to yield better defined Earth models. However, due to the ambiguity between the parameters, even the borehole aided localized tomography

has difficulties resolving a reliable, unique anisotropic model in 3-D (Bakulin et al., 2009).

To further constrain the inversion, we need to consider some prior knowledge of the subsurface. This prior knowledge describes the covariance of the model space, and is independent of the data. There are many ways to obtain the covariance information, based on different assumptions. For example, we often smooth our Earth model horizontally and vertically, which implies a certain user-defined spatial correlation lag. More realistically, we can use the geological information as a priori and shape our estimation accordingly. This model shaping can be posed as a decomposition of the Earth model into different layers and horizons before tomography (Bakulin et al., 2010a), or as a regularization/preconditioning operator during tomography (Bakulin et al., 2010b). We can obtain the geological information either by interpreting and picking the horizons or by building a set of steering filters (Clapp, 2000) according to the current subsurface image.

In addition to the spatial covariance, for a multi-parameter estimation, a local cross-parameter covariance is also needed to better describe the subsurface. One source of the cross-parameter covariance comes from rock physics studies (Hornby et al., 1995; Sayers, 2004, 2010; Bachrach, 2010b). Many authors (Dræge et al., 2006; Bandyopadhyay, 2009; Bachrach, 2010a) have built averaged depth trends serving for seismic processing. In particular, Bachrach (2010a) develops both deterministic and stochastic modeling schemes based on the rock physics effective media models for compacting shale and sandy shale. By making core measurements, we can limit the parameters needed by the rock physics model in a certain range, which greatly reduces the span of the parameter space defined by rock physics modeling. These rock physics modeling results can be used to construct the initial Earth model and the covariance relationships among the Earth model parameters. Li et al. (2011) and Yang et al. (2012) have demonstrated that the rock physics prior models are helpful in constraining ray tomography.

In this paper, we first analyze the topography of the wave-equation migration velocity analysis objective function with respect to different parameterization schemes. To best utilize both surface seismic and rock physics information, we propose a new parameterization scheme for wave-equation migration velocity analysis. For the rock physics modeling, we combine the rock physics models proposed by Bachrach (2010a) and Bandyopadhyay (2009). We model the shale anisotropy from four aspects: mineral anisotropy of the constitutes of the rock, compaction effect on the particle alignment, the transition from smectite to illite due to compaction and temperature, and the lamination effect of isotropic sand layers and anisotropic shale layers. Depth trends (ideally, spatially varying) for the anisotropic parameters from rock physics modeling are obtained from two different sources: seismic inversion results and the well log measurements. We then compare the depth trends in a stochastic manner and the similarity between both depth trends justifies the use of the seismic inversion results in the deeper region that the well log does not cover.

ROCK PHYSICS CONSTRAINED WAVE-EQUATION MIGRATION VELOCITY ANALYSIS FOR ANISOTROPY

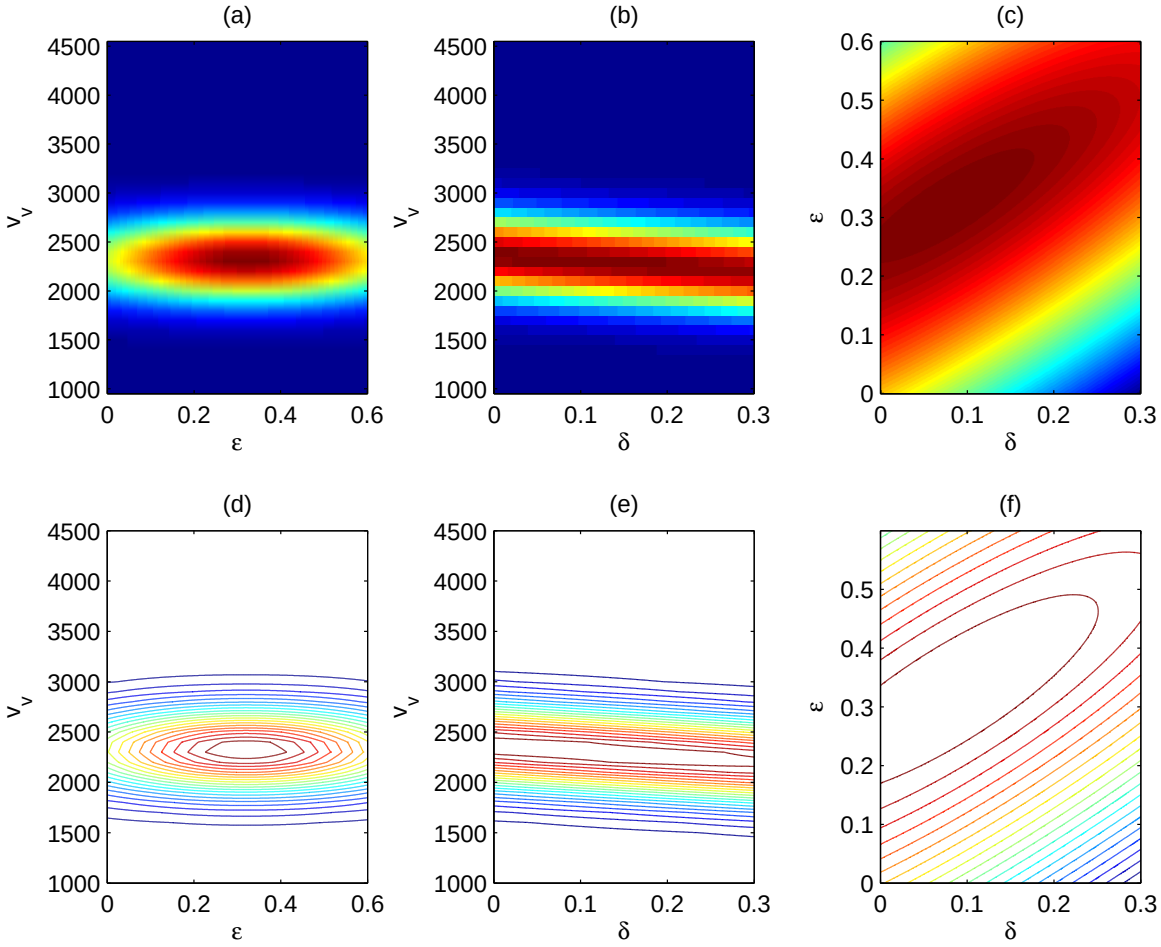

Figure 1: A sketch of the topography of the DSO objective function projected on to (a) v_v-ϵ plane, (b) v_v-δ plane, and (c) ϵ-δ plane. Panels (d), (e), and (f) are the contoured representation of (a), (b), and (c), respectively. [**ER**]

Anisotropic wave-equation migration velocity analysis (WEMVA) aims at building an anisotropic Earth model that minimizes the residual image from the surface seismic data (Li and Biondi, 2011). This optimization problem is highly non-linear and underdetermined. Therefore, we commonly add a regularization term to the anisotropic WEMVA objective function to constrain the null space and stabilize the inversion. The resulting objective function is as follows:

$$S(\mathbf{m}) = \frac{1}{2}||\mathbf{D}_\theta \mathbf{I}(\mathbf{x},\theta)|| + \lambda \frac{1}{2}(\mathbf{m}-\mathbf{m}_{\text{prior}})^T \mathbf{C}_M^{-1}(\mathbf{m}-\mathbf{m}_{\text{prior}}), \tag{1}$$

where the first term is the "data fitting" term, and the second "model regularization" term. In the data fitting term, $\mathbf{m}$ is the anisotropic subsurface model, $\mathbf{I}(\mathbf{x},\theta)$ is the migration image in the angle domain with θ the aperture angle, $\mathbf{D}_\theta$ is a derivative

operator along the angle axis. In the model regularization term, $\mathbf{m}_{\text{prior}}$ and $\mathbf{C}_M$ defines a Gaussian distribution of a prior model, which is ideally independent of the seismic data so that this regularization will bring more information into the optimization. Finally, parameter λ balances the weights between both terms and reflects the confidence of the data compared with the prior model.

The data fitting term, known as differential semblance optimization (DSO) objective function relates the incoherence in the angle domain common image gathers to the inaccuracy in the subsurface models. It has been shown that the traveltimes of qP-waves in TI medium mainly depend on the anellipticity parameter η and the (zero-dip) normal moveout velocity v_n (Alkhalifah and Tsvankin, 1995). In general, the DSO objective function has a much stronger control in velocity (v_v or v_n) than in anisotropic parameters (ϵ and δ). Therefore, we can sketch out the topography of the DSO objective function schematically in figure 1. Notice on the ϵ-δ panel, the better resolved direction is the η direction, more or less parallel to $\epsilon - \delta$ when δ is small. In the unresolved direction, the topography of the DSO objective function is flat.

On the other hand, the topography of the model regularization objective function can be estimated by stochastic rock physics modeling. We will discuss the process of the rock physics modeling in detail in the next section. The resulting topography of the model fitting objective function is shown in figure 2. Compared with the data objective function, the model objective function has much looser control in velocity than in anisotropic parameters. For the Thomsen parameters ϵ and δ, rock physics modeling gives a much tighter distribution.

It is important to note that not only the shape of the distribution is different for both objective functions, the centers of the distribution also differ from each other. When forming a composite objective function by adding the two objectives, both the descending path for the inversion and the final solution to the optimization will be changed. To better utilize both seismic and rock physics information, we should separate the better constrained parameters from the unconstrained parameters, with the emphasis on fitting the seismic data. Therefore, we introduce a new parameter $\eta_\perp$ defined as follows:

$$\eta_\perp = \epsilon + \delta. \tag{2}$$

The direction of $\eta_\perp$ denotes the least constrained direction by the surface P-wave seismic data. We now transform both the topography of the objective functions to the v_n-η-$\eta_\perp$ domain, and the resulting distributions are shown in figures 3 and 4. Notice the topographies for data and model objectives are (nearly) perpendicular to each other. A parameter dependant λ can be used to add appropriate amount of rock physics information to constrain the DSO objective function.

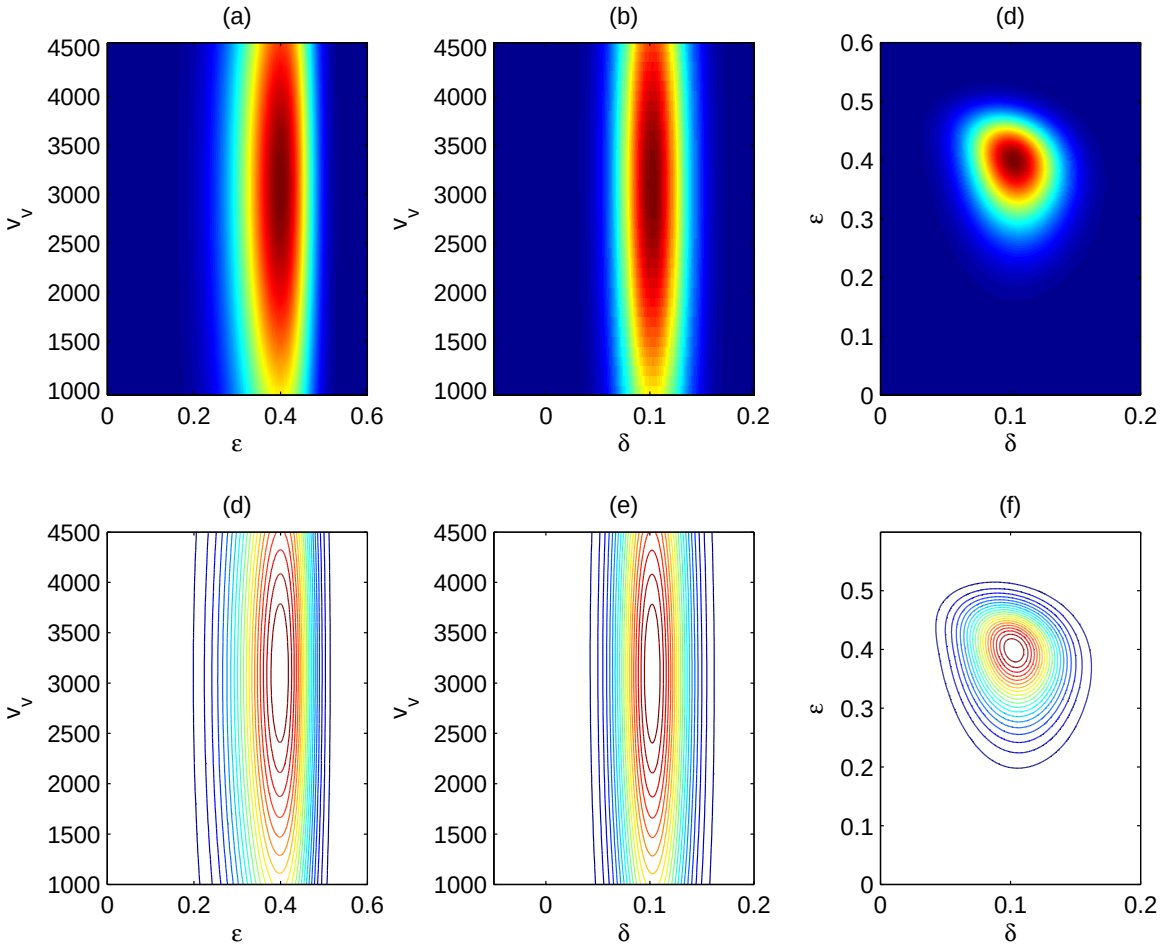

Figure 2: Stocastic rock physics modeling results for parameters v_v, ϵ and δ. Inputs of the rock physics modeling are from seismic inversion results. Topography of the model fitting objective function is projected on to (a) v_v-ϵ plane, (b) v_v-δ plane, and (c) ϵ-δ plane. Panels (d), (e), and (f) are the contoured representation of (a), (b), and (c), respectively. [**ER**]

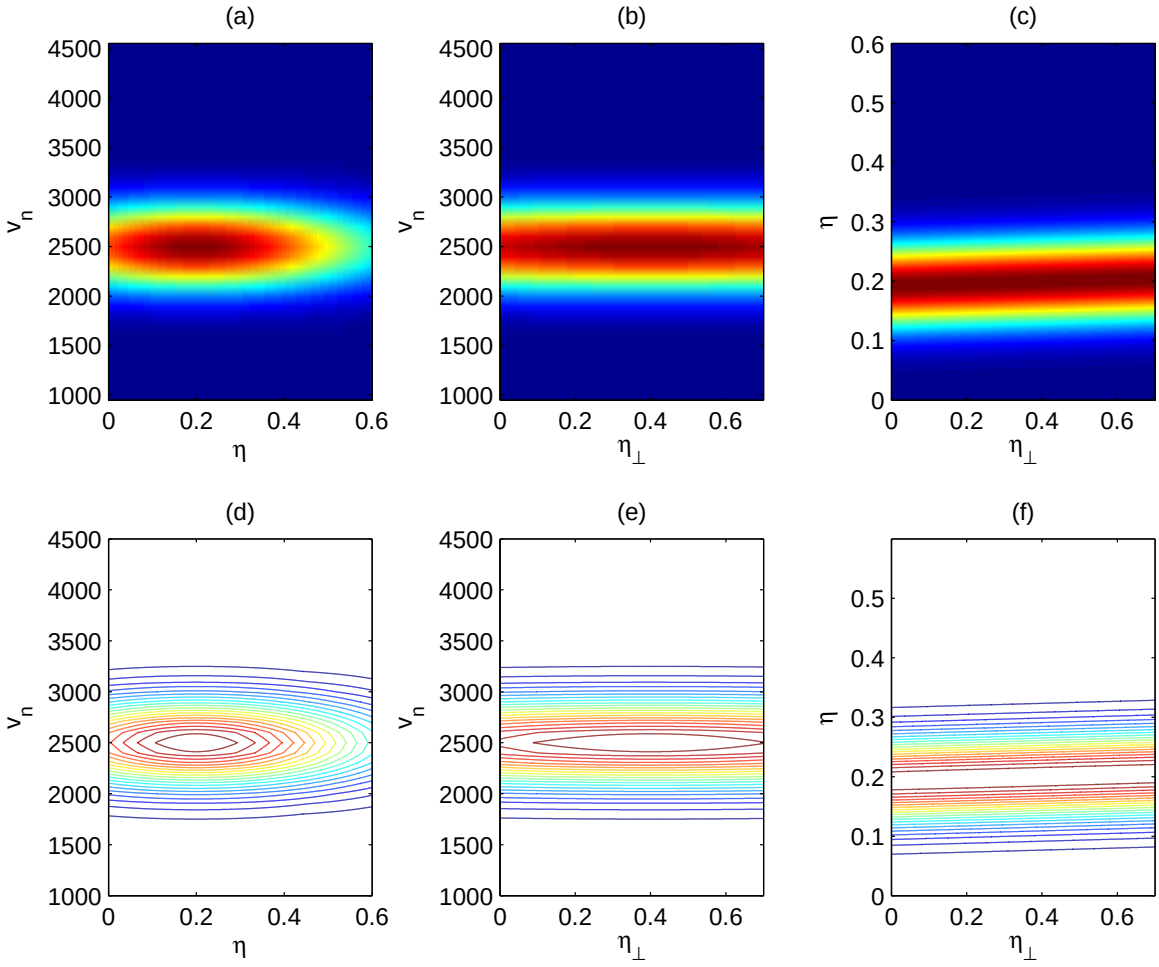

Figure 3: A sketch of the distribution function for the DSO objective function projected on to (a) v_n-η plane, (b) v_n-$\eta_\perp$ plane, and (c) η-$\eta_\perp$ plane. Panels (d), (e), and (f) are the contoured representation of (a), (b), and (c), respectively. [**ER**]

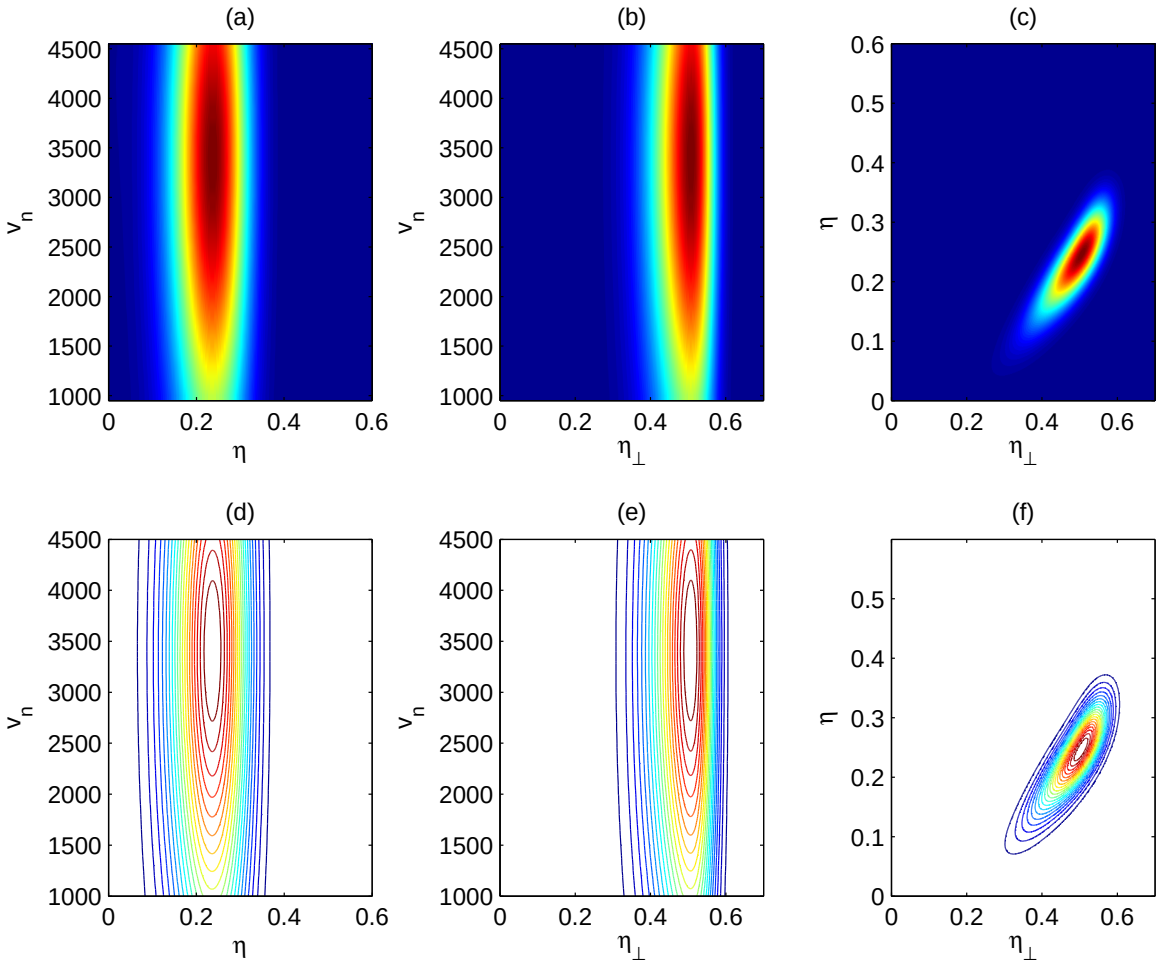

Figure 4: Stocastic rock physics modeling results for parameters v_n, η and $\eta_\perp$. Inputs of the rock physics modeling are from seismic inversion results. Topography of the model fitting objective function is projected on to (a) v_n-η plane, (b) v_n-$\eta_\perp$ plane, and (c) η-$\eta_\perp$ plane. Panels (d), (e), and (f) are the contoured representation of (a), (b), and (c), respectively. [**ER**]

ROCK PHYSICS MODELING FOR SHALE ANISOTROPY

We combine the rock physics models proposed by Bachrach (2010a) and Bandyopadhyay (2009). We model the shale anisotropy from four aspects: mineral anisotropy of the constitutes of the rock, compaction effect on the particle alignment, the transition from smectite to illite due to compaction and temperature, and the lamination effect of isotropic sand layers and anisotropic shale layers. Depth (ideally, spatially varying) trends of anisotropic parameters are obtained.

Mineral anisotropy

We assume shales have three end-member mineral constitutes: smectite, illite and quartz. The elastic properties are listed in table 1. The values of the smectite elasticity are in fact the anisotropic elasticity values for a Cretaceous shale (Hornby et al., 1994). These approximated values are served as an end member when pure shale is fully compacted. Anisotropic elasticity for illite (muscovite) are from work by Wenk et al. (2007). Similar to smectite, although the elasticity of quartz crystal may be anisotropic, we assume an isotropic quartz to approximate the pure sand as an end member in the rock.

Mineral	ρ (g/cc)	v_v (km/s)	v_s (km/s)	ϵ	δ	γ
Smectite	2.4	3.075	1.5	0.255	-0.05	0.48
Illite	2.4	4.94	2.6	1.02	0.	1.68
Quartz	2.65	6.0	4.0	0.	0.	0.

Table 1: Table 1:End-member mineral elastic properties.

Smectite to illite transition

The transition from smectite to illite is a common mineralogical reaction during the burial diagenesis of shales. Many studies (e.g., Hower et al. (1976)) have shown that this transition reaction is controlled by the temperature in the subsurface. In this paper, we follow the work of Bachrach (2010a) to calibrate the percentage of illite P_I to the temperature T as follows:

$$P_I(T) = 0.5 + 0.5 \tanh(\frac{T - T_t}{2\sigma_t}), \tag{3}$$

with T_t the transition temperature and σ_t the width of the transition zone. Reference values $T_t = 58°C$ and $\sigma_t = 60°C$ are from the work of (Freed and Peacor, 1989).

Preferred orientation distribution of clay mineral

Another important factor to the shale anisotropy is the preferred orientation of the clay minerals (Hornby et al., 1994; Sayers, 2004). At initial deposition, mineral domains are oriented in random directions. In this case, even though the individual mineral domain can be anisotropic, the effective medium with randomly oriented domains is isotropic. At the maximum compaction, all the mineral domains are fully aligned, which produces the effective medium with maximum anisotropy.

According to (Bandyopadhyay, 2009), the Voigt averaged stiffness coefficients C^a_{ij} are

$$\begin{aligned}
C^a_{11} &= L + 2M + \frac{4\sqrt{2}}{105}\pi^2(2\sqrt{5}a_3W_{200} + 3a_1W_{400}); \\
C^a_{33} &= L + 2M - \frac{16\sqrt{2}}{105}\pi^2(\sqrt{5}a_3W_{200} - 2a_1W_{400}); \\
C^a_{12} &= L - \frac{4\sqrt{2}}{315}\pi^2(2\sqrt{5}(7a_2 - a_3)W_{200} - 3a_1W_{400}); \\
C^a_{13} &= L + \frac{4\sqrt{2}}{315}\pi^2(\sqrt{5}(7a_2 - a_3)W_{200} - 12a_1W_{400}); \\
C^a_{44} &= M - \frac{2\sqrt{2}}{315}\pi^2(\sqrt{5}(7a_2 + a_3)W_{200} + 24a_1W_{400}); \\
C^a_{66} &= \frac{< C_{11} - C_{12} >}{2},
\end{aligned} \tag{4}$$

where

$$\begin{aligned}
a_1 &= C_{11} + C_{33} - 2C_{13} - 4C_{44}; \\
a_2 &= C_{11} - 3C_{12} + 2C_{13} - 2C_{44}; \\
a_3 &= 4C_{11} - 3C_{33} - C_{13} - 2C_{44}; \\
L &= \frac{1}{15}(C_{11} + C_{33} + 5C_{12} + 8C_{13} - 4C_{44}); \\
M &= \frac{1}{30}(7C_{11} + 2C_{33} - 5C_{12} - 4C_{13} + 12C_{44}),
\end{aligned} \tag{5}$$

with C_{ij} the stiffness coefficients of the individual domain.

In this paper, we use the porosity as an indicator for compaction (Bachrach, 2010a).

$$\begin{aligned}
W_{200}(\phi) &= W^{\max}_{200}(1 - \phi/\phi_0)^m, \\
W_{400}(\phi) &= W^{\max}_{400}(1 - \phi/\phi_0)^n,
\end{aligned} \tag{6}$$

with ϕ the porosity at depth and ϕ_0 the critical porosity. Choice of exponents m and n has not been well studied. We refer to Bachrach (2010a) and let both parameters vary between 0.5 and 2.

Lamination of sand and shale: Backus average

At depth, seismic wavelengths can get as large as a few hundred meters. These long-wavelength seismic waves cannot resolve individual layers, but interacts with the subsurface as a single averaged medium. Elastic properties of an effective medium composed of fine-scale laminations of sand and shale can be described by the Backus average. We assume the sand layer contains pure sand and the shale layer contains pure smectite and illite. Backus (1962) showed that the elastic constants of the effective medium can be obtained by the elastic constants of the individual layers as follows:

$$\begin{aligned} C_{11} &= < c_{13}/c_{33} >^2 / < 1/c_{33} > - < C_{13}^2 > + < c_{11} >; \\ C_{12} &= C_{11} - < c_{11} > + < c_{12} >; \\ C_{13} &= < c_{13}/c_{33} >^2; \\ C_{33} &= < 1/c_{33} >^{-1}; \\ C_{44} &= < 1/c_{44} >^{-1}, \end{aligned} \tag{7}$$

where $< . >$ indicates the averages of the enclosed properties weighted by their volumetric proportions. The volumetric proportions for each lithological components are calculated from the shale content and the percentage of illite. These enclosed properties can be averaged values over orientation distribution functions for shales.

Workflow

Our anisotropic rock physics modeling follows the workflow described here:

- Compute the percentage of illite in the rock given a temperature model.
- Compute the average stiffness coefficients for smectite and illite, given a porosity model.
- Compute the volumetric percentage for each of the mineral phase, given a volumetric percentage of shale.
- Compute the stiffness coefficients for the laminated effective medium.

At each instance of the modeling, the key parameters: ϕ_0, exponents m and n, T_t, and σ_t are varied in a certain range. Therefore, assembly of models, instead of a single model are obtained. These models will be the source of the prior rock physics covariance.

MODELING RESULTS

In the previous section, we define the inputs of our modeling process: a temperature model, a porosity model and a shale content model. The temperature model is relatively smooth in space and is approximated using a typical temperature gradient in the Gulf of Mexico (GoM). Figure 5(c) shows the temperature profile in the shallow water GoM. For the porosity model and the shale content model, we have two different sources: seismic inversion results and the well logs.

An initial isotropic processing work flow has been applied on the field data by Schlumberger. Seismic inversion results, such as, P-wave velocity, shale content, and porosity are also provided. The validation between the porosity inversion result and the well log measurements at the well location suggests that the porosity inversion from seismic is not reliable, probably due to the lack of low frequencies in the seismic data. However, the inversion result for shale content is comparable to the well log measurements. Therefore, we use the provided shale content inversion cube (figure 5(d)) but modeled a smoothly varying porosity trend (figure 5(b)) from the P-wave velocity cube (figure 5(a)).

Using the input in figure 5 and varying the key parameters in the rock physics modeling experiments, we can obtain multiple realizations of the anisotropic parameters in 3-D space. Figure 6 shows one realization of the stochastic modeling experiments. It is interesting to note that parameter ϵ is mainly controlled by the shale content of the subsurface, whereas parameter δ is primarily controlled by compaction and temperature of the subsurface.

Figure 7 shows the topography of the model fitting objective function from the stochastic rock physics modeling using seismic inversion results. The results are shown at three different depth levels: 1 - 2 km in figure 7(a), 2 - 3.5 km in figure 7(b) and 3.5 - 5 km in figure 7(c). In general, the topography for model fitting objective function gets wider as the target gets deeper. Nevertheless, the topography from rock physics modeling is much tighter than the one from seismic data.

We can also extract the input models from the well logs. Figure 8 shows the log measurements and the deduced models for the rock physics modeling. The conversion for gamma ray measurements G to shale content P_{sh} is a simple linear stretch as follows:

$$P_{sh} = \frac{G - G_{min}}{G_{max} - G_{min}}, \tag{8}$$

where G_{min} and G_{max} are the minimum and maximum gamma ray measurements in the log.

Figure 9 shows the topography of the model fitting objective function from the stochastic rock physics modeling using well log measurements. The results are shown at the same three depth levels as in figure 7. We can see that the centers of the distribution in figure 9 are slightly shifted and the distributions are more stretched compared with figure 7. Nonetheless, the general similarity in the shape and the

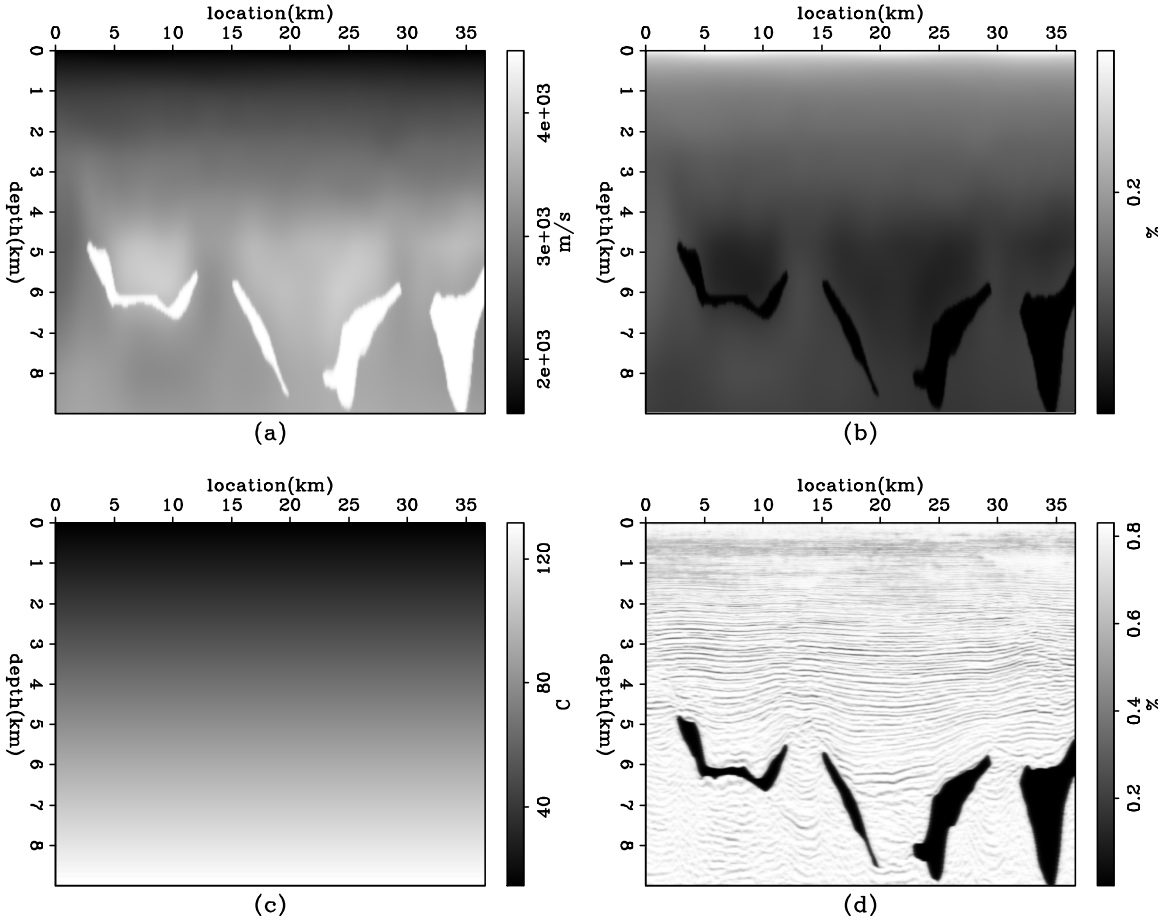

Figure 5: Input of the rock physics modeling from seismic inversion results: (a) velocity profile, (b) porosity profile, (c) temperature profile, and (d) shale content profile. [**ER**]

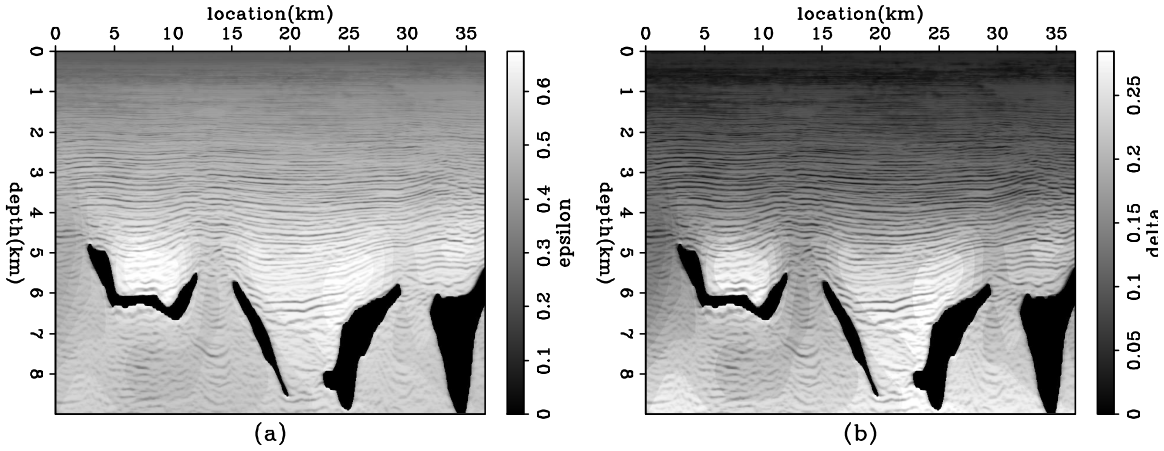

Figure 6: One realization of a 3-D rock physics modeling experiment. (a) modeling result for ϵ; (b) modeling result for δ. [**ER**]

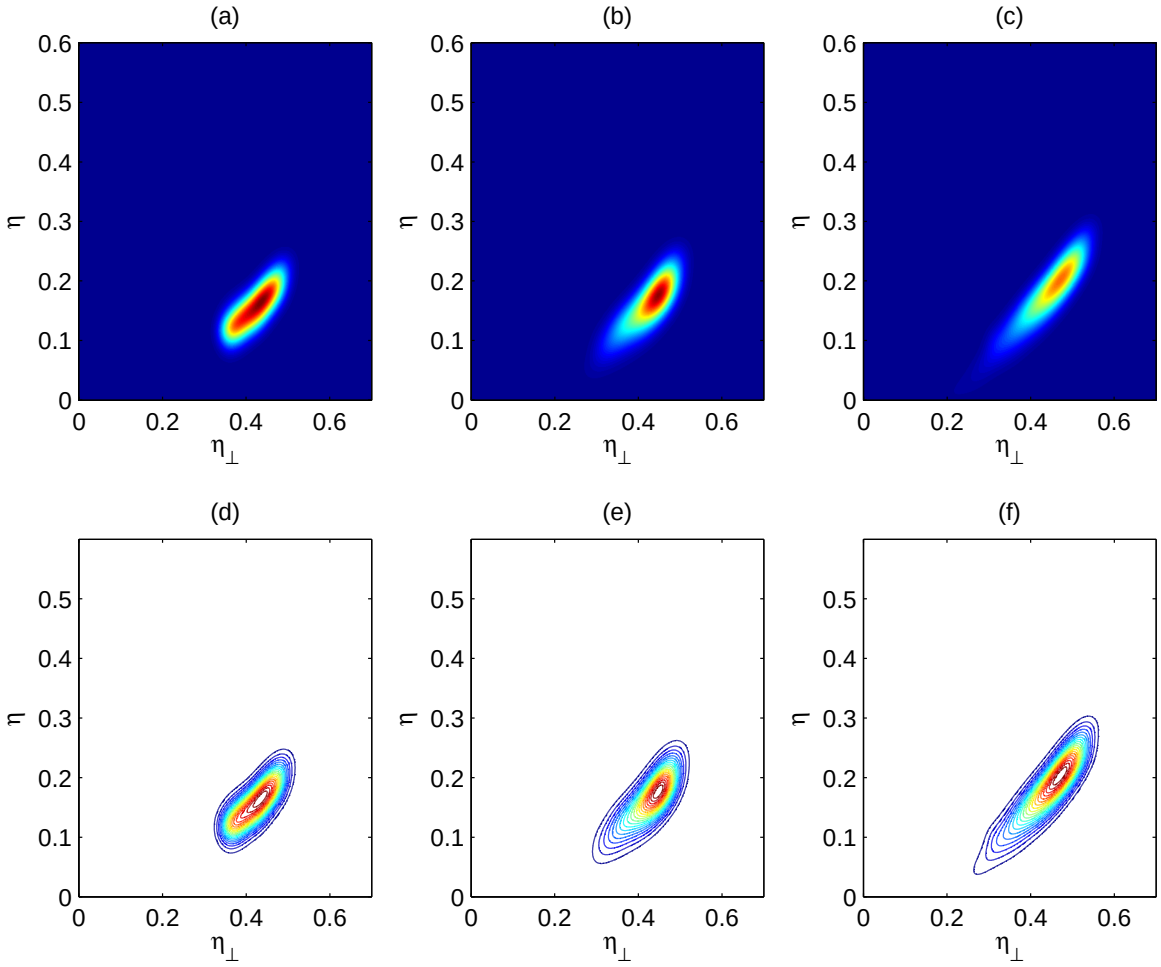

Figure 7: Stochastic rock physics modeling results for parameters v_n, η and $\eta_\perp$. Inputs of the rock physics modeling are from seismic inversion results in figure 5. [**ER**]

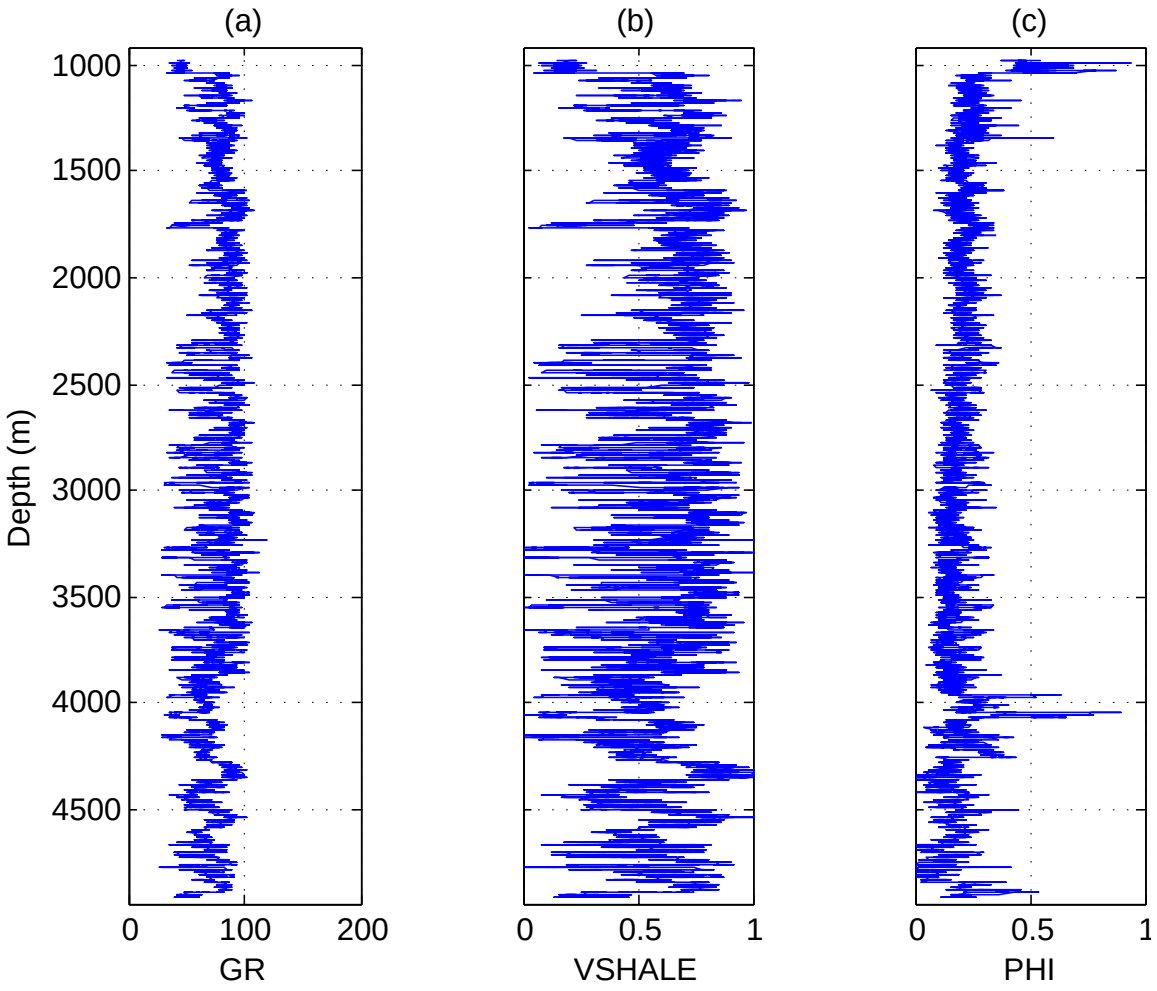

Figure 8: Input of the rock physics modeling from well log measurements: (a) gamma ray measurements, (b) deduced shale contents from gamma ray and (c) porosity. [**ER**]

orientation of both modeling results justify the use of the seismic inversion results and provide confidence when we use only the seismic information in deeper parts that the well log does not covered.

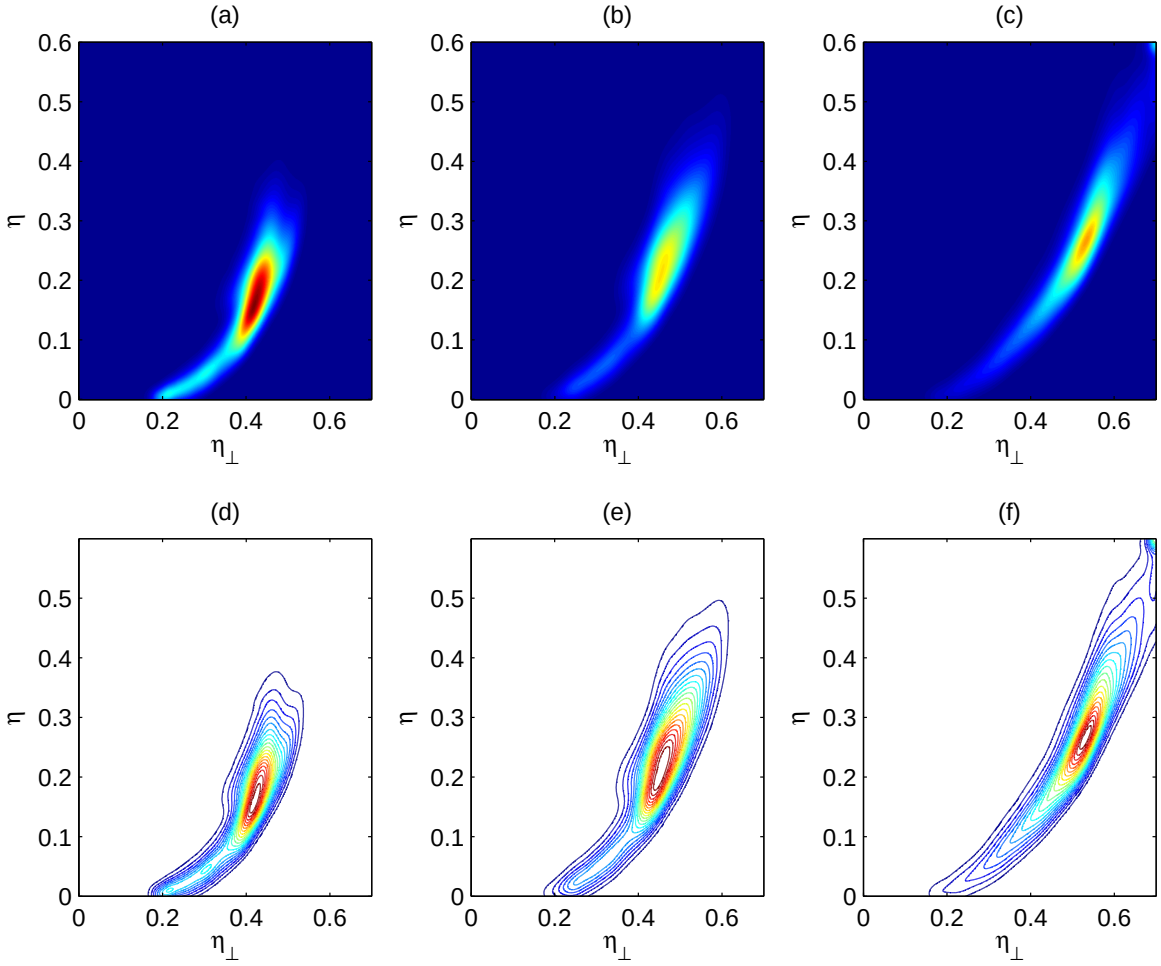

Figure 9: Stocastic rock physics modeling results for parameters v_n, η and $\eta_\perp$. Inputs of the rock physics modeling are from well log measurements. [**ER**]

We approximate the topography of the objective function (1) by adding the rock physics model PDF to the data PDF with a weighting parameter λ. Due to the low resolution of the rock physics modeling to velocity, we only show the topography projected onto the η - $\eta_\perp$ plane. We use the seismic inversion results as the input for rock physics modeling to study deeper subsurface. Figure 10 shows the unconstrained DSO topography with some constraint on η but nearly no constraint on $\eta_\perp$. The topography for the DSO objective function becomes wider as angle coverage of the subsurface gets narrower in the deeper subsurface.

Figure 11 shows the topography of the rock physics constrained objective function (1) when $\lambda = 0.01$. By adding rock physics information, the center of the topography has moved, mostly along the unconstrained direction $\eta_\perp$. Since the data objective function has higher confidence in η, adding rock physics information does not change

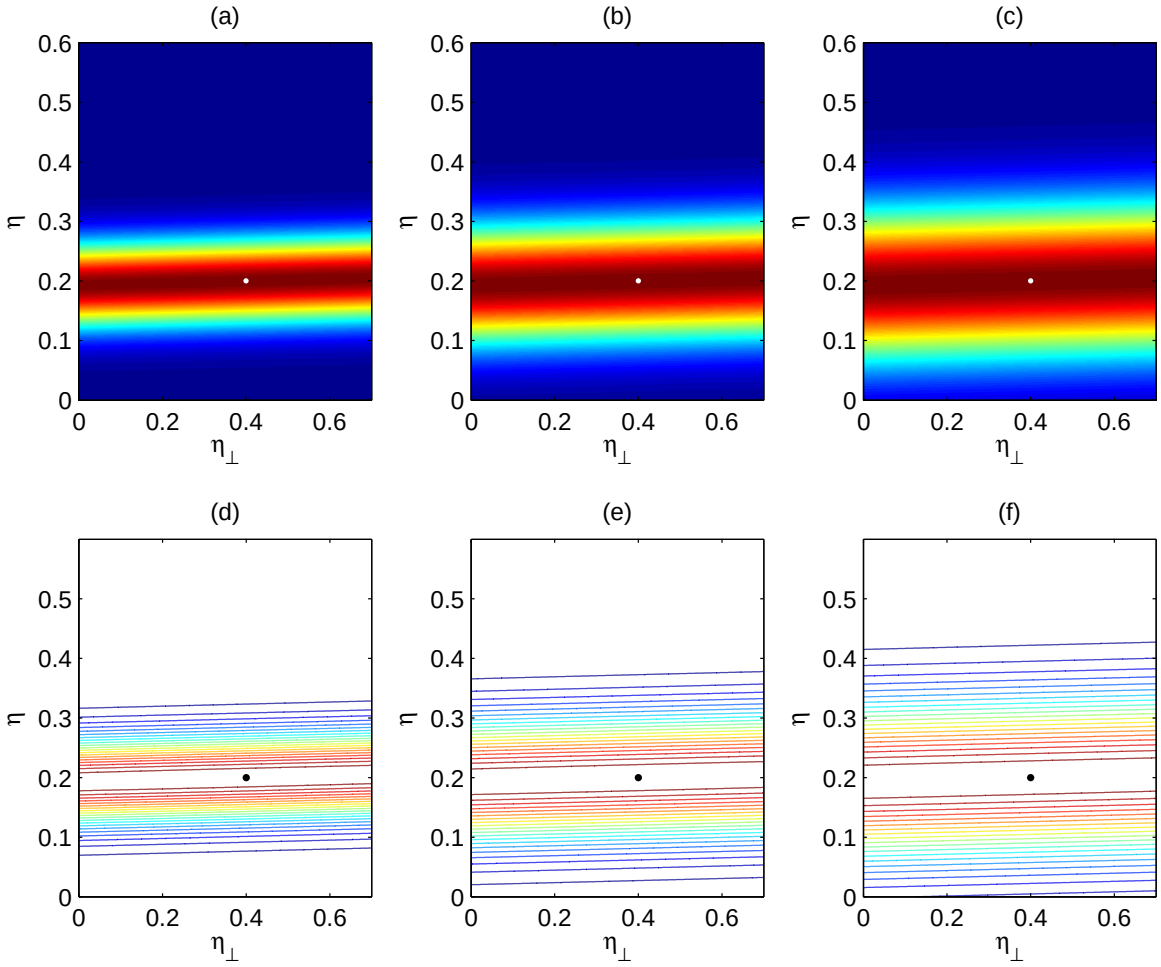

Figure 10: Topography of the DSO objective function in the η - $\eta_\perp$ plane in three different depth levels: (a) $0-3$ km, (b) $3-5$ km and (c) $5-7$ km. [**ER**]

the solution of η in the shallow- and mid-depth. This suggests that this regularization scheme in the shallow subsurface will not change the flatness of the gathers, but will change the positioning of certain reflectors and hence provide different interpretations. On the other hand, in the deeper subsurface where seismic data do not have good constraints to either η or $\eta_\perp$, the solutions are dominated by the rock physics prior information.

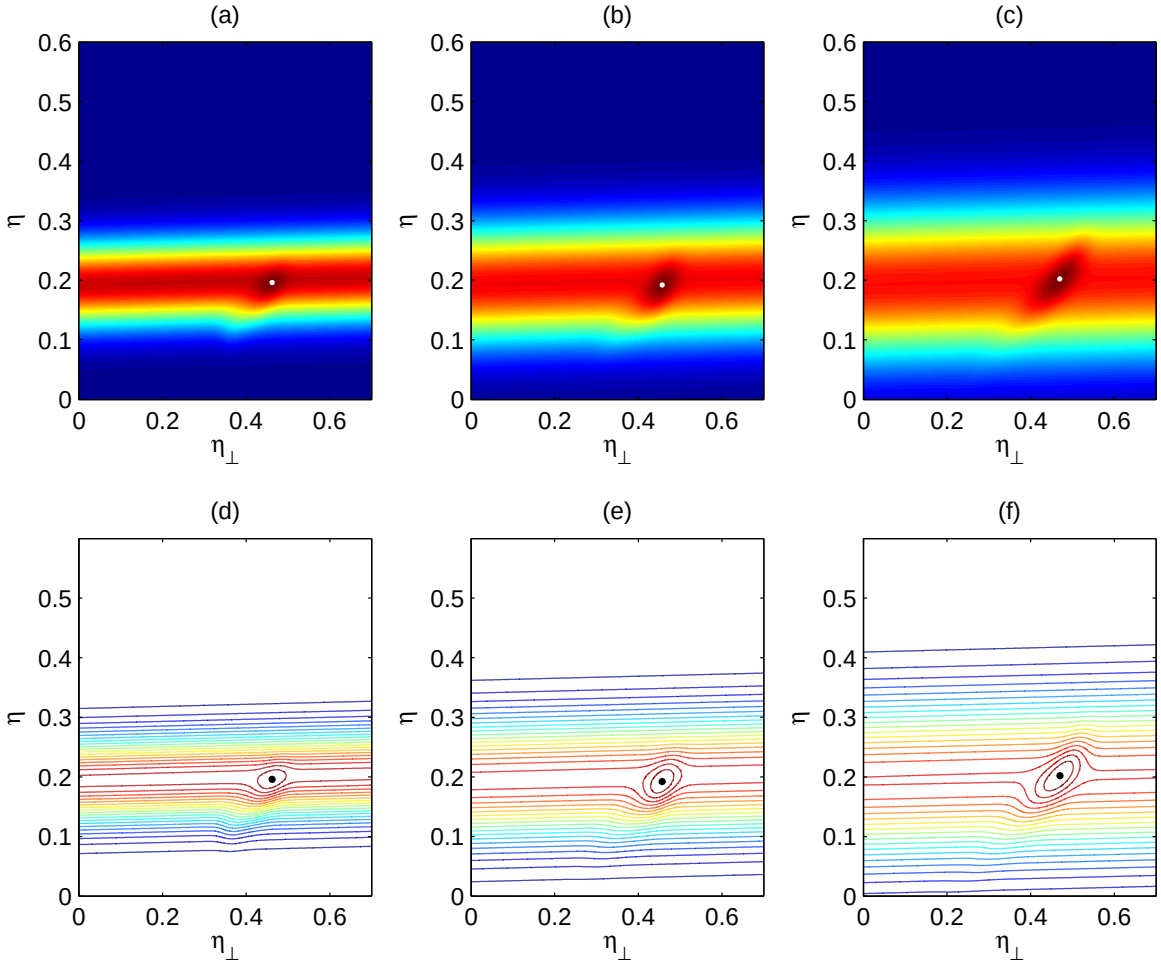

Figure 11: Topography of the regularized objective function with $\lambda = 0.01$ in the η - $\eta_\perp$ plane in three different depth levels: (a) $0-3$ km, (b) $3-5$ km and (c) $5-7$ km. [**ER**]

CONCLUSIONS AND DISCUSSION

In this paper, we study the topography of the image-space DSO objective function with respect to velocity and anisotropic parameters. We show that due to the lack of constraints on the anisotropic parameters, other sources of information are needed to stabilize the inversion.

We combined the rock physics modeling workflow of Bandyopadhyay (2009) and Bachrach (2010a) to study the anisotropic properties of shales. Four different aspects of shale anisotropy are considered: mineral anisotropy, mineralogical transition between smectite and illite due to compaction and temperature, preferred orientations of the clay domain, and finally the lamination of sand and shale.

The stochastic rock physics modeling procedure is repeated with two different sources of inputs: seismic inversion results and well log measurements. Seismic inversion results cover large 3-D space with low resolution and low confidence, whereas the well log measurements provide localized information with high confidence. Stochastic rock physics modeling results from both information sources are compared. The similarity between both results justifies the use of seismic inversion results in the deeper subsurface where well log does not provide coverage. However, more uncertainties should be added in the shale volumetric content and porosity in the deeper region.

From the topography of the constrained objective function for anisotropic parameters, we show that adding rock physics information does not change the solution of the well-constrained parameter by the seismic data. However, valuable information is added where parameters are poorly constrained by the surface seismic data.

The effort of using previous seismic inversion results to constrain the seismic model building in the next iteration helps us to close the loop from seismic data to reservoir modeling. Traditional processing from seismic data to a reservoir model does not include feedback; and the seismic data modeled from the inverted reservoir model usually do not match the field data. Our study is a step along the way to build a closed loop from exploration to production. We hope to recover an Earth model that is consistent with all the available data we have.

ACKNOWLEDGMENTS

The authors thank Schlumberger-WesternGeco for the field dataset. This paper includes data supplied by IHS Energy Log Services; Copyright (2013) IHS Energy Log Services Inc.

REFERENCES

Alkhalifah, T. and I. Tsvankin, 1995, Velocity analysis for transversely isotropic media: Geophysics, **60**, 1550–1566.

Bachrach, R., 2010a, Applications of deterministic and stochastic rock physics modeling to anisotropic velocity model building: SEG Expanded Abstracts, **29**, 2436–2440.

———, 2010b, Elastic and resistivity anisotropy of compacting shale: Joint effective medium modeling and field observations: SEG Expanded Abstracts, **29**, 2580–2584.

Backus, G., 1962, Long-wave elastic anisotropy produced by horizonal layering: Journal of Geophysical Research, **76**, 4427–4440.

Bakulin, A., Y. K. Liu, O. Zdraveva, and K. Lyons, 2010a, Anisotropic model building with wells and horizons: Gulf of mexico case study comparing different approaches: The Leading Edge, **29**, 1450–1460.

Bakulin, A., M. Woodward, Y. Liu, O. Zdraveva, D. Nichols, and K. Osypov, 2010b, Application of steering filters to localized anisotropic tomography with well data: SEG Expanded Abstracts, **29**.

Bakulin, A., M. Woodward, D. Nichols, K. Osypov, and O. Zdraveva, 2009, Can we distinguish TTI and VTI media?: SEG Expanded Abstracts, **28**, 226–230.

———, 2010c, Building tilted transversely isotropic depth models using localized anisotropic tomography with well information: Geophysics, **75**, 27–36.

———, 2010d, Localized anisotropic tomography with well information in VTI media: Geophysics, **75**, 37–45.

Bandyopadhyay, K., 2009, Seismic anisotropy: geological causes and its implications: PhD thesis, Stanford University.

Clapp, R., 2000, Geologically constrained migration velocity analysis: PhD thesis, Stanford University.

Dræge, A., M. Jakobsen, and T. A. Johansen, 2006, Rock physics modeling of shale diagenesis: Petroleum Geoscience, **12**, 49–57.

Freed, R. L. and D. R. Peacor, 1989, Variability in temperature of the smectite/illite reaction in Gulf coast sediments: Clay Minerals, **24**, 171–180.

Hornby, B., D. Miller, C. Esmersoy, and P. Christie, 1995, Ultrasonic-to-seismic measurements of shale anisotropy in a North Sea well: SEG Expanded Abstracts, **14**, 17–21.

Hornby, B. E., L. M. Schwartz, and J. A. Hudson, 1994, Anisotropic effective-medium modeling of the elastic properties of shales: Geophysics, **59**, 1570–1583.

Hower, J., E. Eslinger, M. Hower, and E. Perry, 1976, Mechanism of burial metamorphism of argillaceous sediments: 1. Mineralogical and chemical evidence: Bulletin of The Geological Society of America, **87**, 725–737.

Li, Y. and B. Biondi, 2011, Migration velocity analysis for anisotropic models: SEG Expanded Abstract, **30**, 201–206.

Li, Y., D. Nichols, K. Osypov, and R. Bachrach, 2011, Anisotropic tomography using rock physics contraints: 73^{rd} EAGE Conference & Exhibition.

Sayers, C., 2004, Seismic anisotropy of shales: What determines the sign of Thomsen's delta parameter?: SEG Expanded Abstracts, **23**, 103–106.

———, 2010, The effect of anisotropy on the Young's moduli and Poisson's ratios of shales: SEG Expanded Abstracts, **29**, 2606–2611.

Wenk, H.-R., I. Lnardelli, H. Franz, K. Nihei, and S. Nakagawa, 2007, Preferred orientation and elastic anisotropy of illite-rich shale: Geophysics, **72**, E69–E75.

Yang, Y., K. Osypov, R. Bachrach, M. Woodward, O. Zdraveva, Y. Liu, A. Fournier, and Y. You, 2012, Anisotropic tomography and uncertainty analysis with rock physics constraints: Green Canyon case study: SEG Expanded Abstract, 1–5.